A high-granularity plastic scintillator tile hadronic calorimeter with APD readout for a linear collider detector

V. Andreev[a], J. Cvach[b], M. Danilov[c], E. Devitsin[a], V. Dodonov[d], G. Eigen[d,*,1], E. Garutti[d], Yu. Gilitzky[c], M. Groll[e], R.-D. Heuer[e], M. Janata[b], I. Kacl[b], V. Korbel[d], V. Kozlov[a], H. Meyer[e], V. Morgunov[c], S. Němeček[b], R. Pöschl[d], I. Polák[b], A. Raspereza[d], S. Reiche[e], V. Rusinov[c], F. Sefkow[d], P. Smirnov[a], A. Terkulov[a], Š. Valkár[f], J. Weichert[b], J. Zálešák[b]

[a]*Lebedev Physics Institute, Moscow, Russia*
[b]*Institute of Physics, Academy of Sciences of the Czech Republic, Prague, Czech Republic*
[c]*Institute of Theoretical and Experimental Physics, Moscow, Russia*
[d]*DESY, Hamburg, Germany*
[e]*University of Hamburg, Germany*
[f]*Faculty of Mathematics and Physics, Charles University, Prague, Czech Republic*

Abstract

We report upon the performance of an analog hadron calorimeter prototype, where plastic scintillator tiles are read out with wavelength-shifting fibers coupled to avalanche photodiodes. This prototype configuration has been tested using a positron beam at DESY with energies between 1 and 6 GeV. We present different detector calibration methods, show measurements for noise, linearity, and energy resolution and discuss gain monitoring with an LED system. The results are in good agreement with our simulation studies and previous measurements using silicon photomultiplier readout.

PACS: 07.20.Fw; 29.40.Vj; 29.40.Wk; 42.81.Pa; 42.81.Qb

Keywords: Hardonic calorimeter; Plastic scintillator title; APD readout; Linear collider detector

1. Introduction

The physics requirements at the International Linear Collider (ILC) place high demands on calorimetry [1]. Utilizing the new concept of particle flow, our goal is to achieve a jet-energy resolution of $30\%/\sqrt{E}$ [2–4]. Thus, both electromagnetic showers and neutral hadron showers have to be identified and measured well. The essential requirement is high granularity both in the longitudinal and transverse directions. For the electromagnetic calorimeter, the presently favored option is a silicon–tungsten sandwich calorimeter, while for the hadron calorimeter both analog and digital options are pursued [5,6]. Thus, R&D efforts have started around various laboratories to study the different options.

The analog option of the hadron calorimeter consists of a steel plastic scintillator tile sandwich calorimeter [7]. High granularity is achieved with small plastic scintillator tiles. The light of each tile is collected by a wavelength-shifting (WLS) fiber that is inserted into a groove and is coupled to a silicon photomultiplier (SiPM), a newly developed photodetector [8], or a conventional avalanche photodiode (APD). The performance of 108 SiPMs in a hadronic-calorimeter technical prototype using $5 \times 5\,\mathrm{cm}^2$ plastic

*Corresponding author. Department of Physics, University of Bergen, Allegaten 55, 5007 Bergen, Norway. Tel.: +47 5558 2861; fax: +47 5558 9440.

E-mail addresses: gerald.eigen@ift.uib.no, gerald.eigen@desy.de (G. Eigen).

[1]On leave of absence from University of Bergen, Norway.

scintillator tiles has been published recently [9]. In the present article we report upon the performance of the same technical prototype that is now read out with 33 APDs.

APDs are long-tested photodetectors that have a very high quantum efficiency in the entire spectrum from blue-light to the infrared. Particularly, the APD sensitivity is excellently matched to the green light emitted by the WLS fiber. An APD is typically operated with a gain of a few hundreds, which is about 3–4 orders of magnitudes smaller than that of a SiPM. Thus, an additional preamplifier close to the APD is needed to record the signal with the same data acquisition system. However, due to an increase in noise the observation of low-intensity signals becomes more difficult for APD readout than for SiPM readout. APDs do not suffer from saturation effects and perform reliably, if they are kept at stable reverse-bias voltage and constant temperature. With a good gain-monitoring system any voltage or temperature-induced gain changes can be corrected for. Though the presently tested APDs are too bulky to provide a workable option for a compact high-granularity design, in which each tile needs to be read out separately, our results provide a proof of principle for an analog hadron calorimeter with APD readout. Since we observe minimum ionizing signals from individual tiles with an excellent signal-to-noise ratio and since 1 mm^2 APDs exist, APD readout may become a viable option for the analog hadron calorimeter.

The article is organized in the following way. After summarizing our measurements of different properties of the APDs on a test bench in Section 2, we discuss the layout and operation of the small hadron calorimeter prototype in Section 3. Section 4 presents the simulation of electromagnetic showers in the prototype showing the simulated longitudinal and transverse shower evolution in comparison to our measurements. Section 5 shows our linearity and energy resolution measurements obtained with two different, especially developed preamplifiers in comparison to the simulation and the results with the SiPM readout. Finally, a conclusion and outlook are given in Sections 6 and 7, respectively.

2. Measurements of APD properties

2.1. Detector description

The APDs are specially produced photodetectors from Hamamatsu (S 8664-55 special) with a thin photosensitive area of $3 \times 3\,mm^2$ surrounded by a guard ring. They are reversely biased with voltages up to 425 V reaching gains of a few hundred. The capacitance of these APDs in the undepleted state is about 500 pF. In the fully-depleted state at voltages above 300 V, the capacitance drops to a constant value of 30 pF. To ascertain stable operations and to utilize an optimal dynamic range of our data acquisition system we have operated the APDs at gains of ~100 and ~250 (see Section 2.5). We have monitored the performance of the APDs with an LED system throughout each set of measurements. For each data set, temperature-induced gain changes, however, were rather small, since the run time for calibration plus the energy measurements was a just few hours (see Section 3.4).

2.2. Homogeneity measurements

For a readout of three tiles with one APD as originally planned (see Section 3), it is important to have a homogeneous response in the entire sensitive area. Thus, we have measured the homogeneity of 21 APDs in the laboratory. An APD was fixed on a moving table covered with a light-tight box. Light of a blue LED was guided via a clear cladded fiber (0.5 mm in diameter) to a specific position on the APD, for which we measured the pulse height. Starting at the rim outside the guard ring, we performed a scan in steps of 0.5 mm across the two diagonal lines, yielding 16 representative measurements. Fig. 1a shows the results of a typical scan for a single APD, where we plot the measured pulse heights normalized to the APD average calculated from the 10 measurements having full coverage. Note that the positions 1, 8, 9 and 16 lie outside the sensitive area, while positions 2 and 10 have only partial coverage. While statistical errors are negligible, systematic uncertainties (keeping the same air gap and angle between fiber and APD) are of the order of 5%. Fig. 1b shows the combined results of relative pulse-height measurements inside the sensitive area for all 21 tested APDs. The peak position lies at 1.008 ± 0.003 and has a spread of $\sigma = 0.039 \pm 0.003$. The data demonstrate that all tested APDs are rather homogeneous.

2.3. Gain measurements

The APD gain depends on the reverse-bias voltage and the internal properties of the photodetector. In order to obtain the exact gain dependence, we have tested all 33 APDs at CERN using the APD test setup of the CMS experiment [10]. We have measured the dark current $I_{dark}(U)$ without illumination, the current $I_{total}(U)$ with illumination and the capacitances as a function of the reverse-bias voltage (U) at room temperature (25 °C). Fig. 2 shows the measured gain versus reverse-bias voltage. The observed curves exhibit the expected characteristic shape. The plot indicates that our APDs fall into two groups. About half of the APDs shows the steep gain increase around 421 V with a spread of about ±1 V. For the remaining half of the APDs, the steep gain increase occurs around 425 V with a spread of ±~2 V. The voltage setting of the power supplies was better than 0.1 V.

2.4. Temperature dependence

The APD gain also depends on the operation temperature. We monitor the temperature with three sensors that have an accuracy of 0.05 °C. For small temperature variations the gain changes are linear. We have measured

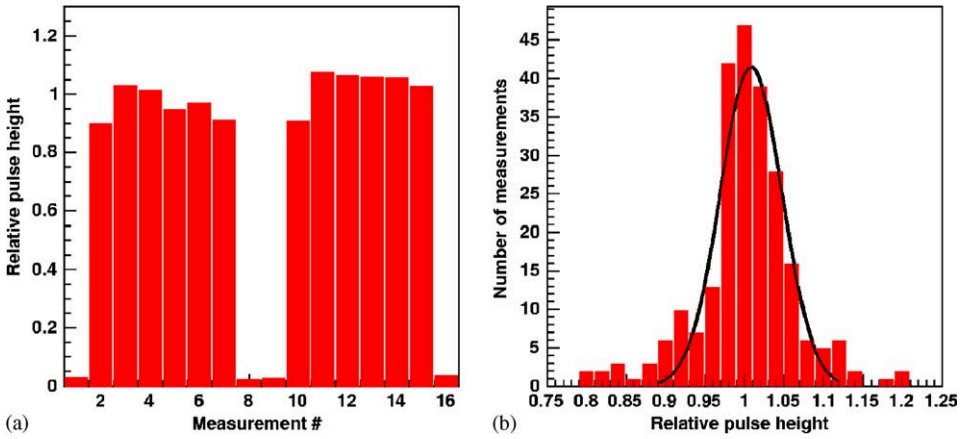

Fig. 1. Relative pulse height measurements of a single APD for 16 positions along the two diagonal lines (a) and the relative pulse height distribution of all measured APD positions inside the sensitive area (b). The measurement procedure is described in the text.

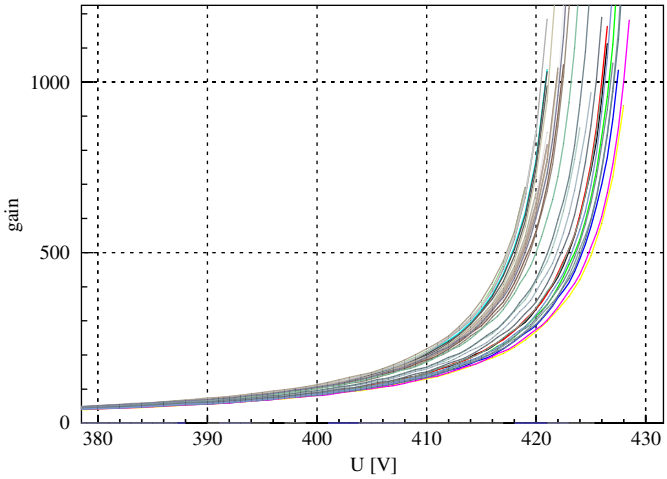

Fig. 2. Measured reverse-bias-voltage dependence of the gain of the 33 APDs used in the prototype.

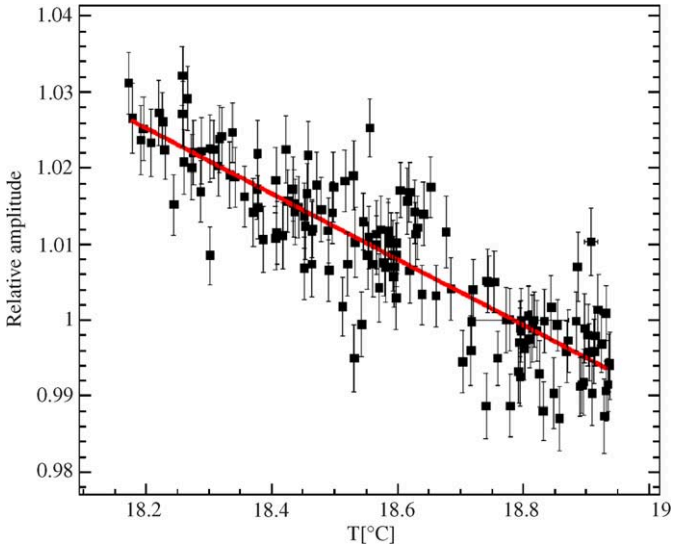

Fig. 3. Temperature dependence of the APD gain in the room temperature range.

this dependence during the monitoring of our testbeam data. The observed gain-temperature correlation of a typical APD read out with the Minsk preamplifier is displayed in Fig. 3 [11]. We found a temperature dependence of $(-4.3 \pm 0.2)\%/^{\circ}\mathrm{C}$ measured in the 18–19 °C temperature range that is consistent with the manufacturer's specification. The accuracy of our gain-monitoring system allows us to correct for gain changes in the data in the offline analysis (see Section 3.4). For example, fitting 150 data points with a Gaussian shape yields an accuracy of the 0.01 °C for the mean value.

2.5. Setup with different preamplifiers

The APD signals were amplified using two types of single-channel preamplifiers: a charge-sensitive preamplifier chip from Minsk and a voltage-sensitive preamplifier from Prague built from discrete components. The two preamplifiers typically operate at gains of $\sim 10^4$ and 2×10^3, respectively. The Minsk preamplifier is superior to the Prague preamplifier with respect to the signal-to-noise (S/N) ratio. It is also smaller in size allowing to place it very close to the APD. Due to operation at 5 V, its dynamic range is limited with respect to that of the Prague preamplifier, which is operated at 10 or 12 V. The Prague preamplifier is superior to the Minsk preamplifier with respect to linearity and crosstalk ($\ll 1\%$), but it has a higher power consumption. Both preamplifiers were coupled to shapers to form the output signal. The shaper of the Prague preamplifier used a second order Bessel approximation for low/high-pass filters. The signal at the output had a rise time of 40 ns and a width of 180 ns for an input signal from the APD. The corresponding values for the Minsk preamplifier were twice as large. Nine preamplifiers were placed on a printed circuit board (PCB). The bias voltage for the APDs could be tuned within $\pm 5\%$ by trimmers. The Prague preamplifier used an input

impedance that was matched with the APD capacitance of 30 pF and had a weak dependence on capacitance.

3. The MiniCal prototype for APD readout

A small sampling calorimeter technical prototype, called the MiniCal, has been built for R&D studies of high-granularity calorimeter readout and operation. The structure consists of 28 layers of 2 cm thick stainless-steel plates. The plates are stacked with 0.9 cm gaps into which thin-walled aluminum cassettes are inserted, each housing nine $5 \times 5\,\mathrm{cm}^2$ wide and 0.5 cm thick plastic scintillator tiles in a 3×3 matrix as shown in Fig. 4. For the beam test, we had equipped only the first 13 gaps with cassettes. We distinguish between tiles with four neighbors, called center tiles, those with three neighbors, called edge tiles, and the remaining ones with two neighbors, called corner tiles. The scintillator material is BC408 from Bicron. Each tile is wrapped with a super-reflector foil (Radiant Mirror film from 3M). The amount of material per layer in terms of radiation lengths and interactions lengths is $1.15\,X_0$ and $0.12\,\lambda$, respectively.

A 60 cm long WLS fiber (double clad Y11-300 from Kuraray) is inserted into a quarter circle groove in the tile. Due to the long attenuation length of the tile and the high reflectivity of the foil, the fiber absorbs most of the scintillation light and reemits isotropically green-shifted light of which a fraction of about 5% is transported to the APD. To optimize the light guide properties of the fiber, an air gap is retained between the plastic scintillator and the fiber. In front of the $3 \times 3\,\mathrm{mm}^2$ active area of the APD, a rubber mask with four holes is used to hold up to three WLS fibers at a fixed place. The fourth hole is used to insert a clear fiber that transports light from a blue LED to monitor the stability of the APD. For practical reasons, all fibers are coupled to APDs via an air gap, since due to the large light yield of approximately 200 photons per APD losses resulting from the air-gap coupling have a minor impact on the performance.

Due to the limited number of available APDs, the original concept consisted in using one APD to read out a group of three tiles located in three consecutive longitudinal layers of our prototype. However, a direct performance comparison with the SiPM readout required also a single-tile readout. Thus, the original concept was modified to read out each of the 13 consecutive center tiles with a single APD, where more than 95% (90%) of the energy of a 1 GeV (6 GeV) electron shower is deposited. The remaining tiles were read out in groups of three as originally planned. This allowed us to equip all edge tiles and tiles in one corner in the first 12 layers with APDs. Since this arrangement used up all 33 APDs, the tiles in the three remaining corners were not read out. This amounts to an energy loss of $<1.5\%$ for the 1–6 GeV energy range.

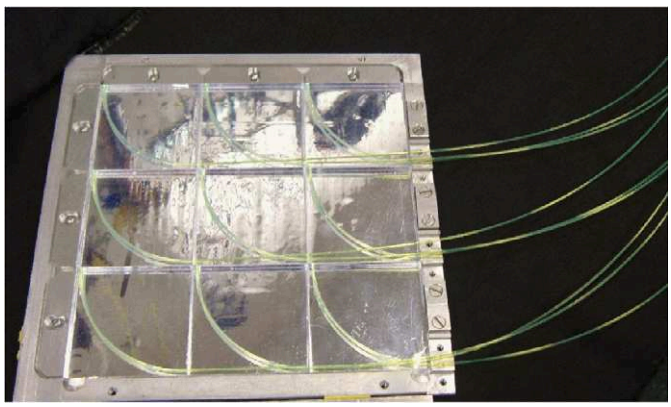

Fig. 4. A MiniCal cassette with nine $5 \times 5\,\mathrm{cm}^2$ plastic scintillator tiles read out by WLS fibers transmitting green light to APDs.

The MiniCal is mounted inside an electrically shielded light-tight box that is positioned horizontally to take test beam data. The box is placed on a moving table allowing to aim the beam at a particular transverse position in the cassette. On one side of the MiniCal box three PCBs are mounted holding sockets for electronics, power supplies and cable connections. The four nine-channel preamplifier units are attached here. The APDs are coupled directly to the preamplifiers grouping them in four arrays holding nine detectors each. The temperature inside the box is monitored by three temperature sensors that are read out by a slow-control system independently from data taking. Further details about MiniCal design, construction and quality control can be found in Ref. [12].

3.1. Signal readout, trigger and data acquisition

Fig. 5 shows a schematics of the signal readout, trigger setup and an LED-based gain-monitoring system. The analog signal output of the APDs is digitized on a 11 bit charge-sensitive ADC (Le Croy 2249W). A CAMAC-based data acquisition is used to collect and store data. A beam trigger is provided by a coincidence of two scintillator finger counter signals. The overlapping area of the counters is $2 \times 2\,\mathrm{mm}^2$. In addition to the beam, LED and random triggers are collected that are produced with a pulse generator operating at a frequency of 1 Hz. A veto signal is provided to the DAQ during the readout time to prevent event pile-up. For the APD gain monitoring, an LED trigger allowed us to take specific LED signals, where the LED pulse amplitude was steerable by a driver card. The stability of the LED signal itself was monitored by a special temperature-stable PIN photodiode.

3.2. Calibration method

For measurements of the shower energy each readout channel (tile–fiber–APD–preamp) needs to be calibrated reliably to account for differences in light yields of the tile–fiber system, APD gains, preamplifier gains and ADC conversions. We have established a robust method using minimum ionizing particles. The energy loss in the plastic scintillator tile is described by a Landau distribution. While the average energy loss depends on the length of the tail,

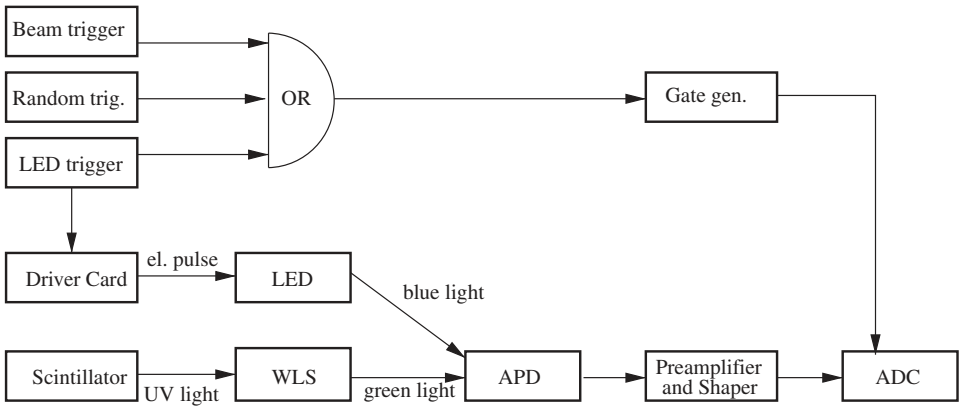

Fig. 5. Schematics of the signal readout, trigger setup and LED-based gain monitoring.

the most probable value is a stable observable. Therefore, we characterize each readout channel in terms of the distance of the peak position (A_{sig}) from the pedestal (A_{ped}), called the MIP peak, MIP $\equiv S = A_{sig} - A_{ped}$. We have calibrated all tiles in the first 12 rows. The center tile in layer 13 was just used as a veto against showering.

To determine the position of the most probable energy loss, we move all cassettes out of the steel absorber inside the light-tight box. A 3 GeV positron beam is aimed at normal incidence at the center of one row of 13 center tiles or 12 edge (corner) tiles. Since the 13 cassettes only have a total of $0.4\,X_0$, the probability of producing secondary particles is rather low. Anyhow, to ascertain that the positron traverses all layers without starting to shower, we require in the offline analysis that the energy loss for center tiles in layer 13 is consistent with that of one minimum ionizing particle. For edge and corner tiles, we check that the last grouped layer is consistent with three MIPs, while for signals in the last grouped layer we impose these requirements on the second-to-last grouped layer, respectively. Since for edge and corner tiles we record the response of three tiles, we use the most probable value of the three-MIP signal as calibration constant. In the energy measurements we also used the three-tile energy sum. Thus, with six distinct beam positions all instrumented channels are calibrated. Taking 25,000 events per channel the entire calibration takes less than an hour. We have performed several calibrations to check for its reliability and stability.

3.3. Data samples

We have performed several shower energy measurements with a positron beam at the DESY test beam facility using both the Minsk preamplifier and the Prague preamplifier at seven different energies (1.0, 1.5, 2.0, 3.0, 4.0, 5.0 and 6.0 GeV). We steered the beam typically at the center of the center tile to ascertain that at least 95% of the total energy was deposited in the row of center tiles. Since the gain of the Minsk preamplifier was about 10^4 and not steerable, the APDs were operated at reverse-bias voltages of $\sim$400 V yielding gains of the order of 100. The gain of the Prague preamplifier was about 2×10^3. The reverse-bias voltage of the APDs, therefore, was set to values around 417 V, typically yielding gains of around 250. We summed the energy deposited in the first 11 layers, in order to be able to compare our results with those obtained with SiPM readout. Even though it is a negligible effect, the energies of the last grouped layers for outer and edge tiles were corrected by a factor of two-thirds. During the measurement the APD gains were rather stable against temperature and voltage fluctuations (<1 V, $<0.1\,^{\circ}$C). We also performed cross-checks at different positions, different gate widths and at a reverse-bias voltage increased by 5 V.

3.4. Monitoring of the response stability

To study the temperature dependence of the APD and to test the capability of correcting for this effect, we have taken data with LED signals for a period of more than 3 days. Fig. 6a shows the LED signal for the uncorrected data. The spectrum does not reveal a Gaussian shape but rather looks like the overlay of several shifted Gaussian distributions. After correcting both for LED light yield fluctuations with the PIN photodiode response and for temperature variations (see Fig. 3), we obtain the spectrum displayed in Fig. 6b. The spectrum is now consistent with a single Gaussian shape.

We have also monitored the stability of our energy measurements. Fig. 7 shows the relative amplitude of LED triggers taken during the energy measurements, where the normalization is the corrected signal of the first run. While open triangles show the uncorrected data, solid points show the data after corrections for temperature variations and PIN photodiode fluctuations. The uncorrected data show only variations within 1%, since the entire run period covered only a few hours during which temperature changes were small. Nevertheless, after temperature and PIN photodiode corrections we observe a slight improvement.

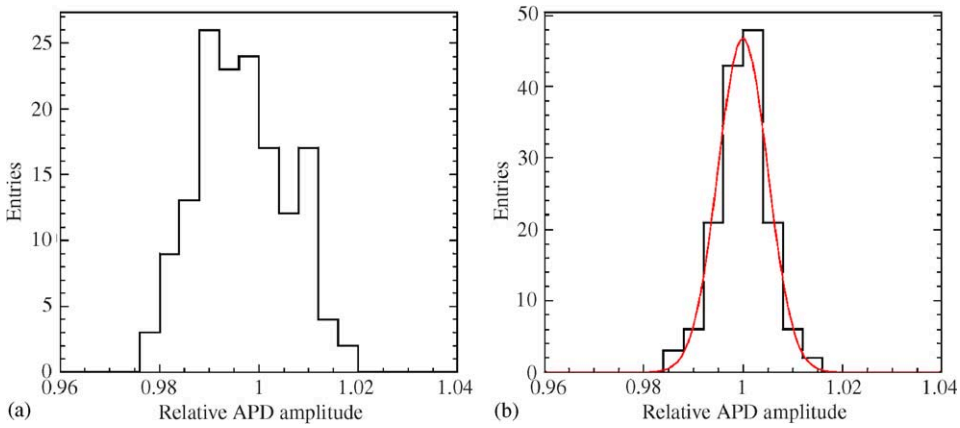

Fig. 6. The relative APD amplitude spectrum for a 3-day running period before (a) and after (b) temperature and PIN diode corrections.

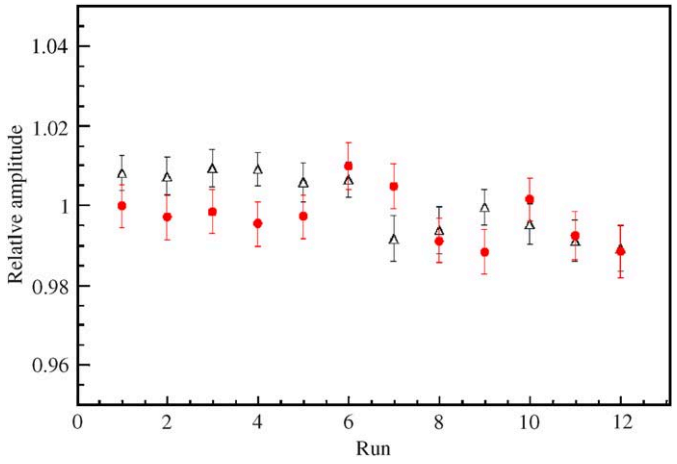

Fig. 7. The relative APD amplitude spectrum before (open triangles) and after (solid points) temperature and PIN diode corrections for a typical run period in the test beam.

4. Monte Carlo simulation

4.1. Monte Carlo technique

The electron shower evolution is simulated with the MiniCal geometry in the GEANT4 [13] framework. For the stainless-steel plates we assume a density of 7.85 g/cm^3. To implement the cassette structure, we consider a 2.5 mm thick aluminum front wall, a 5 mm thick plastic scintillator tile including a WLS-fiber loop, a 1.1 mm thick aluminum backplane and a 0.4 mm wide air gap. A total number of 12 layers of steel and readout cassettes are simulated. In the analysis of the simulated data, however, we have summed up the energy of the first 11 layers only, since this represented the same criteria used in the analysis of the SiPM data.

4.2. MIP simulation

For a realistic simulation of the MiniCal signals, we need to implement the individual physics processes of the readout chain directly: the energy loss in a tile by traversing particles (E_{dep}), conversion of the ionization energy into scintillation light in the plastic scintillator, its collection and reemission in the WLS fiber, transport of the green-shifted light to the APD, conversion of light into photoelectrons, and the measurement of the signal with a charge-sensitive ADC after further amplification and shaping.

In the simulation we divide the readout process into three steps utilizing real data input by comparing the MIP signal characteristics of the calibration runs in data and simulation, where the absorber material is replaced by an air gap. First, we divide the energy deposited in a tile by the energy corresponding to the most probable energy deposition of a minimum ionizing particle, yielding the ratio E_{dep}/MIP. For the MIP deposition, the simulation yields a value of 810 keV. Next, we divide E_{dep}/MIP by the ratio N_{pe}/MIP that is extracted from the MIP signal width in the data. Finally after adjusting the simulated MIP position by comparing it to that in the data, we multiply the simulated value by $N_{\mathrm{ADC}}/N_{\mathrm{pe}}$. Here, we also account for electronic noise by applying Gaussian smearing using the width of the measured pedestal distribution.

We perform this procedure that converts the energy deposition in units of MeV to units of ADC channels for each channel individually to account for differences in the measured light collection efficiencies. Fig. 8 shows the resulting simulated MIP spectrum in comparison to the measured MIP spectrum. The figure confirms that the simulation reproduces our measured spectrum rather well. The conversion of ADC channels back to the number of MIPs is achieved with our calibration procedure channel by channel in a similar way as in the data analysis. To obtain the entire energy deposited by the traversing particle, we sum the individual MIP contributions of all tiles. We take the energy spread of the beam into account as well as fluctuations in the signal detection.

4.3. Shower development

Fig. 9 depicts the development of the electromagnetic shower in the longitudinal direction of the MiniCal. The

energy deposition is expressed in number of MIPs. For each of the first 11 layers in the MiniCal, the measured response of 5 GeV positrons is compared to that in the simulation. The measured spectra are obtained after applying the calibration procedure described in Section 3.2, while the simulation results are obtained after using the procedure described in the previous section. Since this plot presents a direct comparison of individual layers, we correct the energy sum of the last grouped layer in the outer tiles by a factor of two-thirds. The agreement between data and simulation is at the 1% level. For further improvements the individual calibration spectra rather than the mean values need t o be implemented into the simulation. Fig. 10 presents the observed lateral shower shape in comparison to that of the simulation for the fifth layer of the MiniCal. Here, three corner tiles are not shown as they were not equipped with photodetectors. Since the positron shower is essentially contained in the central tiles, leakage effects are small. Both figures demonstrate that the Monte Carlo simulation gives a reasonable description of the shower profiles. The small discrepancy observed in the lateral shower shape results from a slight offset in the beam direction from the center of the center tile, since the cassettes had to be moved in and out of the absorber for calibration purpose.

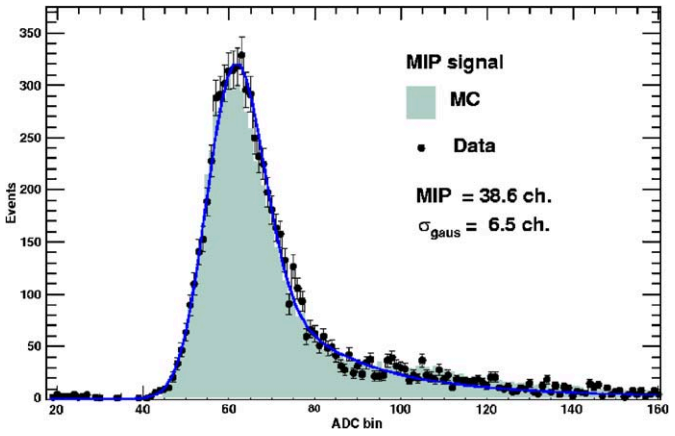

Fig. 8. Comparison of measured and simulated MIP spectra from a single-tile channel recorded with an APD. The data are represented by points with error bars and the Monte Carlo simulation by the shaded histogram. The solid line shows a fit with a Gaussian distribution for the MIP peak plus a Landau distribution for the tail.

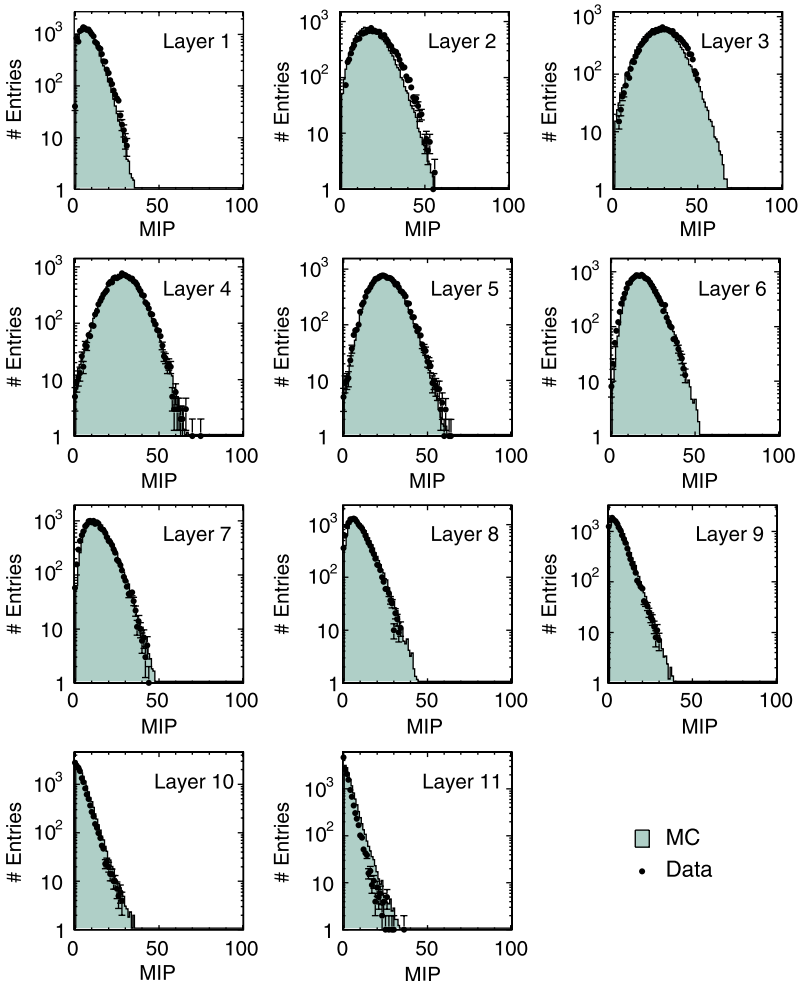

Fig. 9. Development of the electromagnetic shower of 5 GeV positrons in the longitudinal direction in the first 11 layers of the MiniCal. Solid points show the data and the gray-shaded histograms the simulation. The spectra expressed in number of MIPs refer to individual tiles with APD readout.

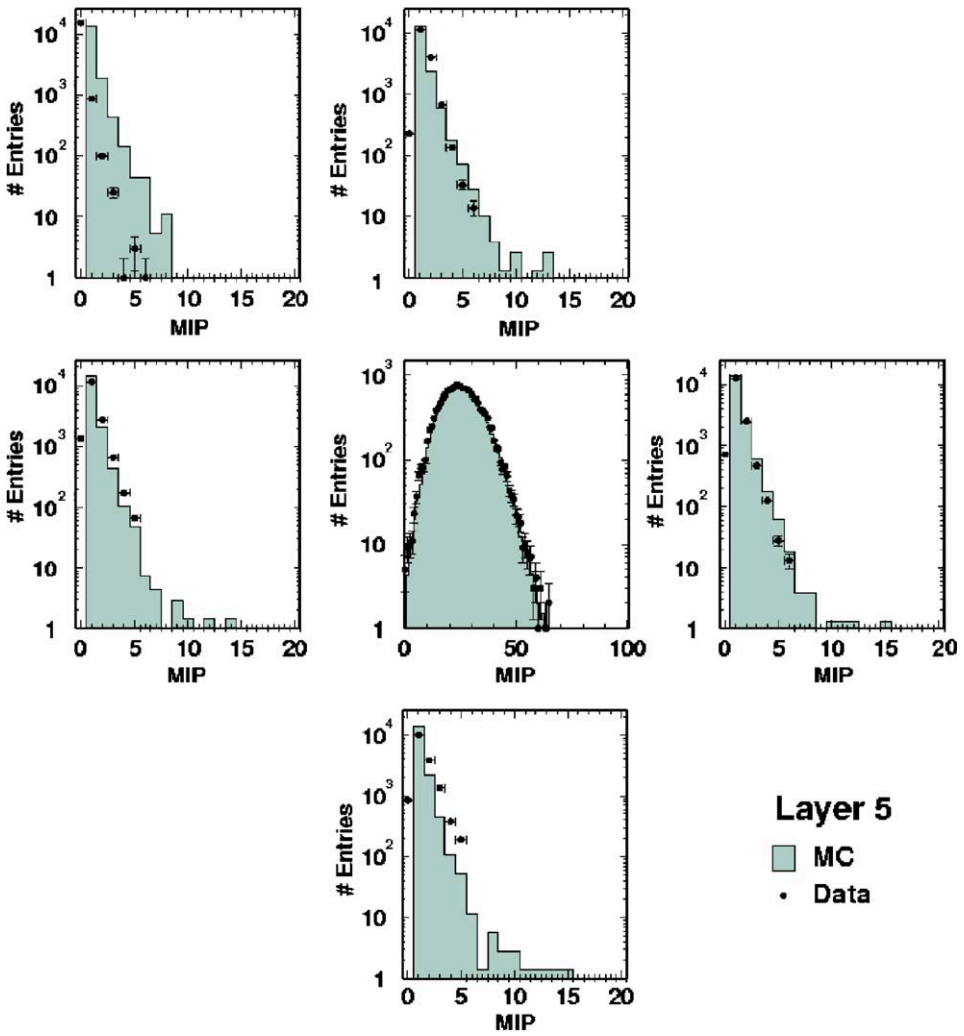

Fig. 10. The lateral shower shape of 5 GeV positrons in the fifth layer of the MiniCal. Solid points show the data and the shaded histograms the simulation in units of MIPs. For the center tile, the distribution shown is the one measured. For the four edge tiles and one corner tile, we divide the observed distribution by three, since it represents a sum over three consecutive tiles. The three corner tiles that were not read out are not shown.

5. Results

5.1. Analysis procedure and calibration results

To determine the calibration constants, we have performed two slightly different offline analyses. In the first analysis, the MIP is determined by a maximum likelihood fit with a Gaussian distribution for the pedestal, a second Gaussian shape for the minimum ionizing peak and a Landau distribution for the high-energy tail. In the second analysis, the MIP position is determined from a maximum likelihood fit using a Gaussian shape for the pedestal plus a second Gaussian shape for the minimum ionizing distribution. To reduce the effect from the Landau tail, only data above the MIP position within one standard deviation are included in the fit. To reduce second-particle effects and thus suppress showering particles, we require a MIP signal in the last readout layer of the MiniCal in the first analysis or MIP signals in two adjacent layers in the second analysis. Both fitting procedures applied on the same calibration data give compatible results at the level of $\sim$1%. This uncertainty is added as a systematic error of the calibration method, see Section 5.4.

Fig. 11 shows typical MIP signal distributions for both data taken with the Minsk preamplifier and data taken with the Prague preamplifier. The overall gain (APD plus preamplifier) in the APD setups is slightly smaller than that of the SiPM readout chain [8]. For each channel, we perform the MIP calibration described in Section 3.2 and store calibration factors. Using this procedure, we measure energy of electromagnetic showers in units of MIPs. The calibration of electromagnetic showers in units of GeV can be obtained from the energy measurements in the test beam.

To characterize and compare the different APD readout systems, we determine the S/N ratio, where S is the MIP amplitude and $N \equiv \sigma_{\mathrm{ped}}$ is the Gaussian width of the pedestal distribution. The S/N ratio is 9.7 ± 2.0 for data

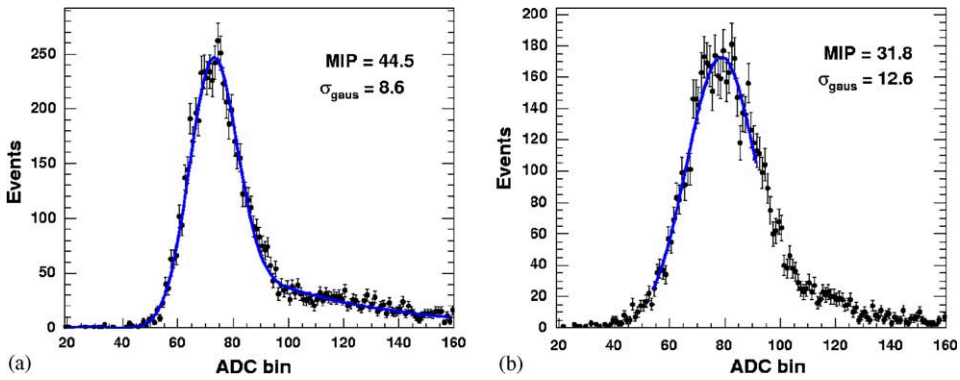

Fig. 11. Typical MIP spectra from measurements of APDs with (a) a Minsk preamplifier and (b) a Prague preamplifier. The displayed quantities are derived from a combined Landau plus Gaussian fit and a simple Gaussian fit, respectively. The widths of corresponding pedestals are $\sigma_{\text{ped}}^{\text{minsk}} = 3.4 \pm 0.7$ bins and $\sigma_{\text{ped}}^{\text{prague}} = 9.7 \pm 0.2$ bins.

read out with the Minsk preamplifier and 3.4 ± 0.7 for data read out with the Prague preamplifier. Generally, the S/N ratio for data with APD readout is worse than that for SiPM readout (see Ref. [9]). The reason is the APD excess noise and an increased pickup noise due to a reduced intrinsic gain of APD.

Another interesting quantity that shows the separability between signal and pedestal is the ratio S/σ_{gauss}, where σ_{gauss} represents the Gaussian width of the MIP signal. This quantity may be useful for setting a minimum requirement on the threshold for separability of the MIP position from the pedestal. Our measurements yield values of 5.1 ± 0.5 for data taken with the Minsk preamplifier and 2.5 ± 0.4 for data taken with the Prague preamplifier. These results are comparable to $S/\sigma_{\text{gauss}} = 3.7 \pm 0.1$ obtained with the SiPM readout.

Note that the position and width of the MIP signal displayed in Figs. 11a and b depend strongly on the APD working point. For example, increasing the reverse-bias voltage on the APD read out with the Prague preamplifier by 5 V at constant temperature yields an enhancement of S/N by $\approx 60\%$ and S/σ_{gauss} by $\approx 30\%$, respectively. Nevertheless, for our calibration procedure the results on linearity and resolution do not change.

5.2. Linearity

Using our analysis procedure described in the previous section, we determine the energy of the electromagnetic shower event by event in units of MIPs. For compatibility with the SiPM results [9], the energy in the central tile of the 12th layer was omitted and the energy of the outer tiles in the last grouped layers was adjusted by a factor of two-thirds. For each beam energy the resulting energy distribution is fitted with a Gaussian line shape to determine the most probable value. Fig. 12 shows the measured MIP positions as a function of the positron beam energy in the 1–6 GeV range for data with the Minsk preamplifier (triangles) and data with the Prague preamplifier (squares). The Monte Carlo prediction for the MiniCal read out with APDs, as described in Section 4, is shown by open points.

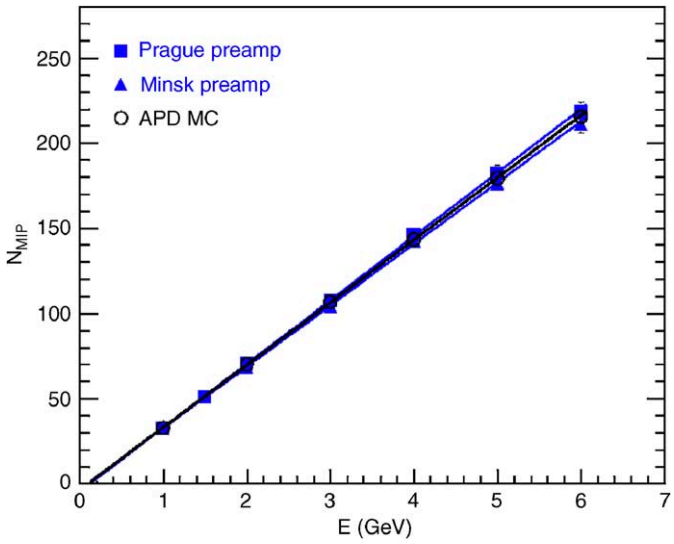

Fig. 12. Linearity measured with the Minsk preamplifier (triangles) and with the Prague preamplifier (squares), respectively. Open points show the Monte Carlo prediction for our APD measurements.

We perform a linear fit to the data to extract the slope parameter in units of MIP/GeV. The measured energies and fitted slopes for two different preamplifiers agree at the level of 3%, which lies within the considered systematic errors (see Section 5.4). By constraining the intercept of the fit to zero changes the slope by 2% (3%) for data taken with the Minsk (Prague) preamplifier with respect to the unconstrained fit. The predicted values from the APD Monte Carlo simulation are in good agreement with the measured results.

5.3. Energy resolution

The energy resolution σ_E/E is derived as the spread of a signal distribution relative to the most probable signal as the function of the beam energy. The measured values for

two data sets are plotted in Fig. 13. For comparison, the Monte Carlo prediction is also shown. The stochastic terms of the energy resolution for both the Minsk and Prague preamplifier data, extracted from maximum likelihood fits, are in excellent agreement. In both data sets, a value of the order of 21% is obtained that agrees well with that of the APD Monte Carlo simulation. The data are not very sensitive to the constant terms which are zero within errors.

5.4. Systematic errors

The errors used in the analysis (Fig. 12 and 13) include both statistical and systematic uncertainties added in quadrature. The statistical errors are typically of the order of 1.0–1.5%. The sources of the systematic uncertainties are listed in Table 1. The uncertainty coming from the difference of two calibration methods (Section 5.2) is about 1% and is proportional to the absolute energy as well as the energy distribution spread and thus cancels in the energy resolution measurement. The main source of systematic errors for the energy resolution measurement is electronic noise (pedestal width), which contributes more significantly at low energies. The application of low-energy thresholds leads to an uncertainty of $\leqslant 2\%$ and affects mainly low energies. Variations of conditions during calibration measurements as well as the energy scans due to temperature and reverse-bias voltage add another contribution of 3%. The nonlinearity in the energy measurement is estimated to be about 4% at the lowest energies. Uncertainties due to the beam energy spread are of the order of 6% at 1 GeV decreasing to 2% above 3 GeV.

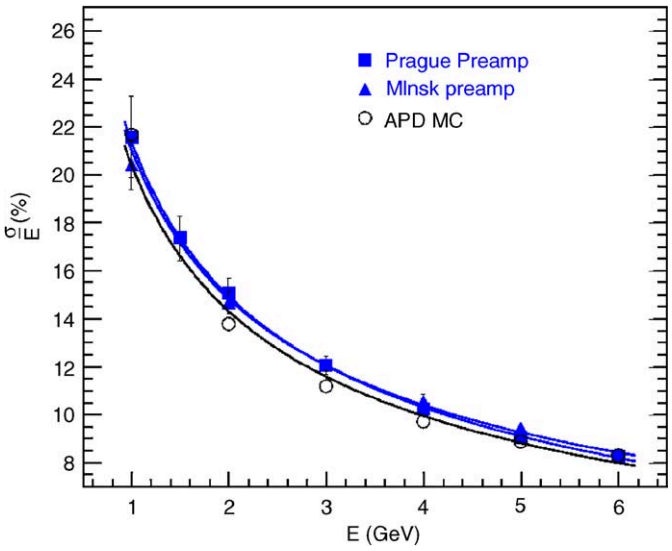

Fig. 13. Energy resolution measured with the Minsk preamplifier (triangles) and with the Prague preamplifier (squares), respectively. Open points show the Monte Carlo prediction for our APD measurements. The fit functions comprise of the stochastic term and a constant term added in quadrature.

Table 1
Individual contributions of systematic uncertainties of the measurements in the test beam

Type	Relative value (%)	Source
Calibration	1	Different calibration methods
Noise	6–1	Electronic noise (width of the pedestal)
Thresholds	2–1	Signal thresholds and cuts
Stability	3	Time stability of calibration
Linearity	4–1	Nonlinearity of ADC

Displayed intervals indicate an energy-dependent systematic error, where the first value refers to 1 GeV and the second value to 6 GeV.

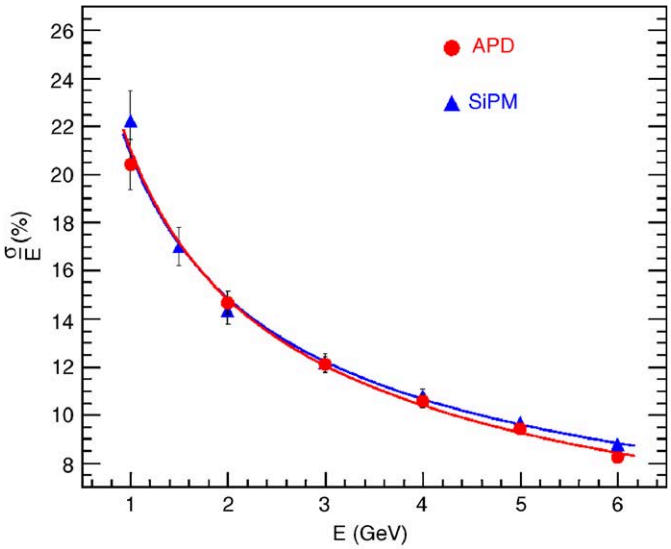

Fig. 14. Measured energy resolution for test beam data of the MiniCal read out with APDs (points) and SiPMs (triangles).

5.5. Comparison of results

The linearity measurements of the APD readout and the SiPM readout agree with each other rather well. Fig. 14 shows the energy resolution measured in the MiniCal with APD readout in comparison to that with SiPM readout. For both setups, we have no sensitivity for measuring the constant term in the energy resolution. The measurements of the stochastic terms are in excellent agreement yielding 21.2 ± 0.7 for the APD (Minsk) readout and 20.7 ± 0.7 for the SiPM readout. Both results are also consistent with the expectation from simulations.

6. Conclusions

We have demonstrated that APDs provide an alternative option to the SiPM readout for an analog plastic scintillator tile calorimeter. Though APDs have a gain that is about four orders of magnitude lower than that of SiPMs, and thus need a preamplifier, the MIP signal is clearly separable from the noise. Our data confirm that both a charge-sensitive and a voltage-sensitive preamplifier yield equivalent performance. The APDs do not suffer

from nonlinearity effects at high-light amplitudes. The quantum efficiency for the emission spectrum of the WLS fiber is about a factor of six higher than that for the SiPM.

For stable operation a gain-monitoring system of the complete readout chain is necessary, since gain fluctuations may occur due to temperature changes and bias-voltage fluctuations. The present study shows that these variations can be reliably corrected for offline. Using a positron test beam with energies ranging between 1 and 6 GeV, we have measured the linearity and energy resolution of an analog hadron calorimeter prototype as a function of energy. The linearity for APD readout with both preamplifier designs is in good agreement. Due to the thick absorber material in our technical prototype, the sampling fluctuations in the shower development are sufficiently large that the difference in the noise spectra of the two preamplifiers is insignificant. The energy resolution we have measured with APD readout is in excellent agreement with that obtained for SiPM readout.

We have developed detailed Monte Carlo simulations to interpret the shape of electromagnetic showers observed in the MiniCal. After adjusting the width of MIP distribution to that observed in the beam calibration, the simulated shower profiles both in the transverse and longitudinal directions are in good agreement with the data. Both the simulated linearity and energy resolution as a function of energy are consistent with our measurements.

7. Outlook

Future R&D will have to prove, if small APDs are suitable for the readout of scintillator tiles in an analog hadron calorimeter. In this concept of reading out the WLS fibers with small APDs, the cassettes have to be designed such to allow a low-noise preamplifier to be placed on the readout board near the APD. Another concept of reading out the plastic scintillator tile directly without the WLS fiber seems feasible with large-area APDs, where the sensitive area is 25–100 times larger than that of a SiPM. Using large-area APDs in conjunction with available scintillators that have long attenuation lengths (≈ 2 m) and super-reflector foils that yield $>99\%$ reflectivity in the blue-light spectrum, we may obtain sufficiently large MIP signals. Independently of the choice of the photodetector, the light output of each channel has to be monitored for stability.

The next step requires a test of the analog scintillator tile calorimeter in a hadron test beam. Based upon the experience obtained with the test beam data, a 1 m^3 large HCAL prototype is under construction that is expected to take data in a hadron beam in 2006/2007 together with an electromagnetic calorimeter prototype and a tail catcher. The data samples taken with this setup will allow us to test the concept of particle flow and will provide us with the final requirements for precision in gain, calibration, noise suppression and MIP identification.

Acknowledgments

We would like to thank the technicians and the engineers who contributed in the design and construction of the prototype. We also gratefully acknowledge the DESY management for its support and hospitality, and the accelerator staff for the reliable and efficient beam operation. This work is supported by the contribution of Bundesministerium für Bildung und Forschung, Germany; Alexander von Humboldt Foundation (Research Award IV, RUS 1066839 GSA), INTAS (Grant # YSF150-00); the Russian grants SS551722.2003.2 and RFBR0402/17307a; the Ministry of Education of the Czech Republic under the project LC527 and INGO-1P05LA259 and by the Grant Agency of the Czech Republic under the project 202/05/0653.

References

[1] TESLA TDR, DESY 2001-011, 2001.
[2] H. Videau, J.-C. Brient, Calorimetry optimized for jets, in: Proceedings of the 10th International Conference on Calorimetry in Particle Physics, Pasadena, World Scientific, Singapore, March 2002, p. 747.
[3] V. Morgunov, Calorimeter design in the energy flow concept, in: Proceedings of the 10th International Conference on Calorimetery in Particle Physics, Pasadena, World Scientific, Singapore, March 2002, p. 70.
[4] F. Sefkow, Performance goals and design considerations for a linear collider calorimeter, in: Proceedings of the 11th International Conference on Calorimetery in Particle Physics, Perugia, March 2004, World Scientific, Singapore, 2005, p. 435.
[5] Memorandum to the PRC, from the proposal 01/02, DESY, Hamburg, Memo-01, CALICE collaboration, October 2001, ⟨http://polywww.in2p3.fr/flc/calice_offic.html⟩.
[6] J. Cvach, Calorimetery at a future e^+e^- collider, Proceedings of ICHEP 2002, Elsevier, Amsterdam, 2003, p. 922.
[7] V. Korbel, A scintillator tile hadron calorimeter for the linear collider detector, Proceedings of Ninth Topical Seminar on Innovative Particle and Radiation Detectors, Siena, 2004.
[8] G. Bondarenko, P. Buzhan, B. Dolgoshein, V. Golovin, E. Guschin, A. Ilyin, V. Kaplin, A. Karakash, R. Klanner, V. Pokachalov, E. Popova, K. Smirnov, Nucl. Instr. and Meth. A 442 (2000) 187.
[9] V. Andreev, et al., Nucl. Instr. and Meth. A 540 (2005) 368.
[10] D. Bailleux, et al., Nucl. Instr. and Meth. A 518 (2004) 622.
[11] This is a two-dimensional plot, since the information is extracted from measurements of temperature versus time with the slow control system and gain versus time with our LED trigger system.
[12] B. Rusinov, The scintillator tile hadronic calorimeter prototype R&D studies and construction plans, Proceedings of Ninth Topical Seminar on Innovative Particle and Radiation Detectors, Siena, 2004.
[13] S. Agostinelli, et al., Nucl. Instr. and Meth. A 506 (2003) 250.